Pergamon

Acta mater. Vol. 45, No. 8, pp. 3163–3179, 1997

Printed in Great Britain
PII: S1359-6454(97)00011-6
1359-6454/97 $17.00 + 0.00

COMPARISON OF DISCRETE DISLOCATION AND CONTINUUM PLASTICITY PREDICTIONS FOR A COMPOSITE MATERIAL

H. H. M. CLEVERINGA[1], E. VAN DER GIESSEN[1]† and A. NEEDLEMAN[2]

[1]Delft University of Technology, Laboratory for Engineering Mechanics, Mekelweg 2, 2628 CD Delft, The Netherlands and [2]Brown University, Division of Engineering, Providence, RI 02912, U.S.A.

(Received 8 October 1996; accepted 18 December 1996)

Abstract—A two-dimensional model composite with elastic reinforcements in a crystalline matrix subject to macroscopic shear is analyzed using both discrete dislocation plasticity and conventional continuum slip crystal plasticity. In the discrete dislocation formulation, the dislocations are modeled as line defects in a linear elastic medium. At each stage of loading, superposition is used to represent the solution in terms of the infinite medium solution for the discrete dislocations and a complimentary solution that enforces the boundary conditions, which is non-singular and obtained from a linear elastic, finite element solution. The lattice resistance to dislocation motion, dislocation nucleation, and dislocation annihilation are incorporated into the formulation through a set of constitutive rules. Obstacles leading to possible dislocation pile-ups are also accounted for. Results are presented for materials with a single slip system. A reinforcement size effect is exhibited by the discrete dislocation-based analysis whereas the continuum slip results are size independent. The discrete dislocation results have higher average reinforcement stress levels than do the corresponding continuum slip calculations. Averaging of stress fields over windows of increasing size is used to gain insight into the transition from discrete dislocation-controlled to continuum behavior. © *1997 Acta Metallurgica Inc.*

1. INTRODUCTION

Much is known about metal plasticity from both the dislocation and continuum points of view [e.g. 1–5]. Physically, plastic deformation in crystalline metals is a consequence of the motion of large numbers of dislocations. The mobility of dislocations gives rise to plastic flow at relatively low stress levels compared to the theoretical strength, although each dislocation is associated with a large local stress concentration. In the continuum approach, plastic deformation at such stress levels is embodied in the constitutive relation, but the local stress concentrations due to the discreteness of dislocations is not accounted for.

Microscale mechanical behavior, including, for example, deformation and failure in metal-matrix composites and plastic flow near crack tips, is often analyzed using continuum plasticity formulations. It is presumed that the stress and deformation fields obtained from such analyses are representative of those in a dislocated solid over some sufficiently large region. However, dislocation-based plasticity has a characteristic length, the Burgers vector, while conventional continuum plasticity is size independent. Additionally, the stress concentrations that arise from heterogeneous dislocation arrangements such as pile-ups or in dislocation-free regions may be of fundamental significance for failure. Therefore, the size of the region over which the continuum description should give a representative characterization of the actual stress state is not clear. The transition from a dislocated solid to a conventional continuum plasticity description is not at all straightforward.

In this paper, we undertake a direct comparison between the response of a dislocated solid and the predictions of continuum plasticity in a simple context. A composite material subject to simple shear is analyzed. Attention is focused on periodic distributions of particles, so that calculations can be carried out for a unit cell. Using discrete dislocation plasticity, results are presented for several arrangements of particles within the unit cell and, for one of the arrangements, for two particle sizes. The same boundary value problems are solved using a phenomenological continuum slip description of plastic flow following the approach of Peirce *et al.* [6]. In both descriptions, single slip is assumed on slip planes parallel to the shear direction. The phenomenological crystal plasticity and discrete dislocation results for the overall stress–strain response and for the local stress distribution are compared.

The framework for analyzing dislocated solids is that of Van der Giessen and Needleman [7, 8], where plastic flow arises directly from the collective motion of large numbers of discrete dislocations. Other approaches to discrete dislocation plasticity modeling have been presented by, for example, Gulluoglu *et al.*

†To whom all correspondence should be addressed.

[9], Amodeo and Ghoniem [10], Kubin *et al.* [11], Gulluoglu and Hartley [12], Fang and Dahl [13] and Groma and Pawley [14]. However, the formulation in Ref. [8] and used here focuses on full boundary value problem solutions for plastically deforming solids. Attention is restricted to small strains with the dislocations being modeled as line defects in an isotropic linear elastic solid. Following Lubarda *et al.* [15], the stresses and strains are written as superpositions of fields due to the discrete dislocations, which are singular inside the body, and complimentary fields that enforce the boundary conditions and account for interaction with second-phase particles. This leads to a linear elastic boundary value problem for the smooth complimentary fields which is solved by the finite element method. Thus, the long-range interactions between dislocations are accounted for through the continuum elasticity fields. Drag during dislocation motion, interactions with obstacles, and dislocation nucleation and annihilation are also accounted for. These are not represented by the elasticity description of dislocations and are incorporated into the formulation through a set of constitutive rules.

In our formulation the plastic stress–strain response and the evolution of the dislocation structure are outcomes of the boundary value problem solution. By way of contrast, in a continuum formulation the plastic stress–strain response is an input, whereas dislocation analyses typically postulate a dislocation structure [16, 17].

In the following, vectors and tensors are denoted by bold-face symbols, · denotes the inner product, ⊗ the tensor product and : the trace product. For example, using the summation convention, $\mathbf{a}\cdot\mathbf{b} = a_i b_i$, $(\mathbf{a}\otimes\mathbf{b})_{ij} = a_i b_j$ and $(\mathscr{L}:\mathbf{B})_{ij} = \mathscr{L}_{ijkl}B_{lk}$. The gradient operator on (tensor) fields is denoted by ∇.

2. FORMULATION AND METHOD OF ANALYSIS

The formulation follows that of Van der Giessen and Needleman [8] where the general development is given along with further references. A linear elastic body of volume V is considered that contains elastic reinforcements with volume V^* and has a distribution of dislocations in the matrix material $V^M = V/V^*$ [see Fig. 1(a)]. The elastic properties of the matrix material are characterized by the fourth-order tensor $\mathscr{L}$ and the elastic properties of the reinforcement by $\mathscr{L}^*$. The dislocations are treated as line defects in the elastic continuum [1, 2].

The computation of the deformation history, assuming small strain kinematics, is carried out in an incremental manner. Each time step involves three main computational stages: (i) determining the current stress and strain state for the current dislocation arrangement; (ii) determining the forces between dislocations, i.e. the Peach–Koehler force; and (iii) determining the rate of change of the dislocation structure, which involves the motion of dislocations, the generation of new dislocations, their mutual annihilation, and their pinning at obstacles.

2.1. *The current stress and strain state*

The method for determining the current state of the body with the current dislocation distribution is an extension of the formulation of Lubarda *et al.* [15]. The key idea is illustrated in Fig. 1. The current state of the body in terms of the displacement, strain and stress fields is written as the superposition of two fields:

$$\mathbf{u} = \tilde{\mathbf{u}} + \hat{\mathbf{u}}, \quad \epsilon = \tilde{\epsilon} + \hat{\epsilon}, \quad \sigma = \tilde{\sigma} + \hat{\sigma} \quad \text{in } V, \quad (1)$$

respectively. The (˜) fields are the superposition of the fields of the individual dislocations, in their current configuration, but in an infinite medium of the

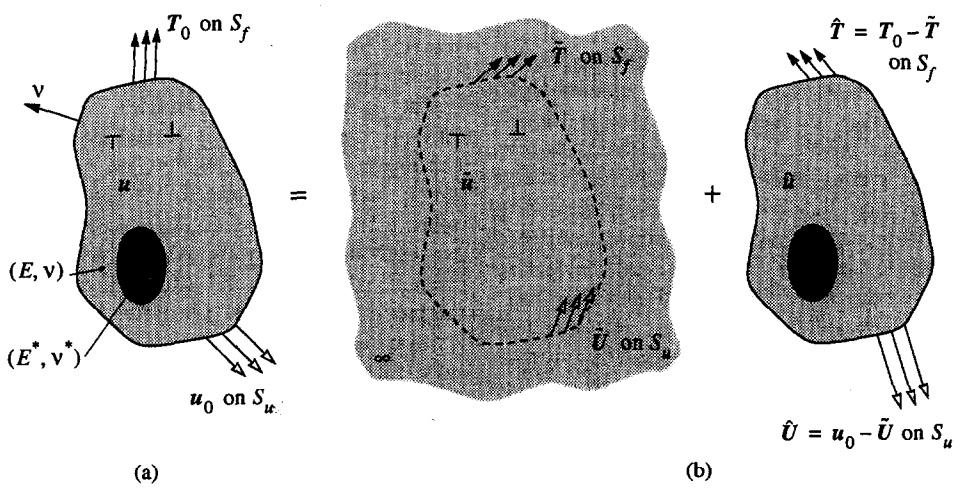

Fig. 1. (a) Definition of the boundary value problem for a dislocated body with elastic inclusions. (b) Decomposition into the problem of interacting dislocations in the homogeneous infinite solid (˜ fields) and the complementary problem for the non-homogeneous body without dislocations (ˆ fields).

homogeneous matrix material, and are obtained by superposition of the fields $(\mathbf{u}^i, \boldsymbol{\epsilon}^i, \boldsymbol{\sigma}^i)$ associated with the individual dislocations,

$$\tilde{\mathbf{u}} = \sum_i \mathbf{u}^i, \quad \tilde{\boldsymbol{\epsilon}} = \sum_i \boldsymbol{\epsilon}^i, \quad \tilde{\boldsymbol{\sigma}} = \sum_i \boldsymbol{\sigma}^i \quad (i = 1, \ldots, n) \tag{2}$$

where n is the number of dislocations in the current configuration. The $(\tilde{\ })$ fields give rise to tractions $\tilde{\mathbf{T}}$ and displacements $\tilde{\mathbf{U}}$ on the boundary of the body.

The $(\hat{\ })$ fields represent the image fields that correct for the actual boundary conditions on S and for the presence of the particles. The governing equations for the $(\hat{\ })$ fields are

$$\left.\begin{aligned} \nabla\cdot\hat{\boldsymbol{\sigma}} &= \mathbf{0} \\ \hat{\boldsymbol{\epsilon}} &= \nabla \otimes \hat{\mathbf{u}} \end{aligned}\right\} \text{in } V = V^{\mathrm{M}} \cup V^{*} \tag{3}$$

$$\begin{aligned} \hat{\boldsymbol{\sigma}} &= \mathscr{L}:\hat{\boldsymbol{\epsilon}} && \text{in } V^{\mathrm{M}} \\ \hat{\boldsymbol{\sigma}} &= \mathscr{L}^{*}:\hat{\boldsymbol{\epsilon}} + (\mathscr{L}^{*} - \mathscr{L}):\tilde{\boldsymbol{\epsilon}} && \text{in } V^{*} \end{aligned} \tag{4}$$

$$\begin{aligned} \boldsymbol{\nu}\cdot\hat{\boldsymbol{\sigma}} &= \hat{\mathbf{T}} = \mathbf{T}_0 - \tilde{\mathbf{T}} && \text{on } S_{\mathrm{t}} \\ \mathbf{u} &= \hat{\mathbf{U}} = \mathbf{u}_0 - \tilde{\mathbf{U}} && \text{on } S_{\mathrm{u}}. \end{aligned} \tag{5}$$

Here, S_{t} is the portion of the boundary on which tractions are prescribed, S_{u} is the portion of the boundary on which displacements are prescribed, $\mathbf{T}_0$ and $\mathbf{U}_0$ are the prescribed traction and displacement vectors, respectively, and $\boldsymbol{\nu}$ is the outer unit normal to S. Symmetry of stress and strain tensors is implicitly assumed in (4) and (5). A key point is that the $(\hat{\ })$ fields are smooth, so that equations (3)–(5) constitute a conventional linear elastic boundary value problem that can be conveniently solved by the finite element method.

Both the matrix material and the reinforcement material are taken to be isotropic. The elastic moduli for the matrix can be written in the form

$$\mathscr{L} = 2\mu\left[\mathbf{I}' + \frac{\nu}{1-2\nu}\mathbf{I}\otimes\mathbf{I}\right] \tag{6}$$

where μ is the shear modulus, ν is Poisson's ratio, and $\mathbf{I}$ and $\mathbf{I}'$ are the second- and fourth-order identity tensors, respectively. A similar expression holds for the reinforcement moduli with μ replaced by μ^* and ν by ν^*.

2.2. *Boundary value problem*

Calculations are carried out for a two-dimensional model composite material containing rectangular particles arranged in a hexagonal packing, as illustrated in Fig. 2. We identify a unit cell of width $2w$ and height $2h$ $(w/h = \sqrt{3})$ which contains two particles of size $2w_{\mathrm{f}} \times 2h_{\mathrm{f}}$, one being located at the center of the cell. The particles remain elastic, and plasticity is confined to the matrix. The complete material system is obtained by stacking replicas of the cell in a doubly-periodic pattern.

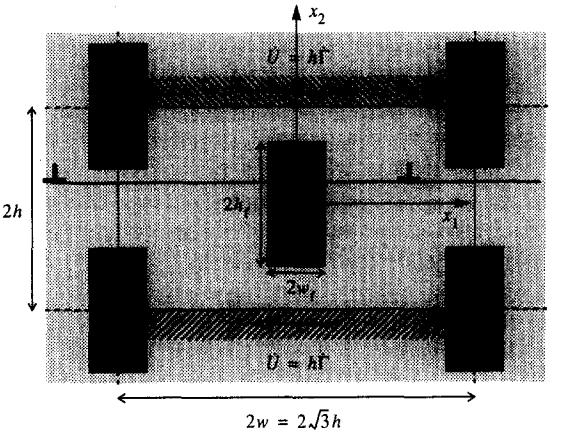

Fig. 2. Unit cell of a composite material with a doubly-periodic array of elastic particles. All slip planes are taken to be parallel to the applied shear direction (x_1).

The cell is subjected to plane strain, simple shear, which is prescribed through the boundary conditions

$$u_{0,1}(t) = \pm h\dot{\Gamma}t, \quad u_{0,2}(t) = 0 \quad \text{along } x_2 = \pm h \tag{7}$$

where $\dot{\Gamma}$ is the applied shear rate. Periodic boundary conditions are imposed along the lateral sides $x_1 = \pm w$. These kinematic boundary conditions constrain the deformation of the particles at the cell vertices (see Fig. 2) to some extent. The average shear stress $\bar{\tau}$ needed to sustain the deformation is computed from the shear component σ_{12} of the total stress $\boldsymbol{\sigma}$, either along the top or the bottom face of the region:

$$\bar{\tau} = \frac{1}{2w}\int_{-w}^{w} \sigma_{12}(x_1, \pm h)\, \mathrm{d}x_1. \tag{8}$$

The finite element discretization of the equations (3)–(5) governing the $(\hat{\ })$ fields, uses four-node quadrilateral elements with 2×2 Gaussian integration. The meshes consist of 102×60 quadrilaterals. The finite element stiffness matrix is formed and factored once; only the loading vector of the discretized equations varies from time step to time step.

We consider glide on a single slip system only, with the slip plane normal $\mathbf{n}$ being in the x_2-direction so that the glide direction $\mathbf{m}$ and the shearing direction coincide. For simplicity, only edge dislocations are considered, all having the same magnitude b of the Burgers vector.

2.3. *The forces between dislocations*

Assuming dislocation glide only, the variation of the potential energy of the body due to infinitesimal variations of the position of the ith dislocation is governed by the Peach–Koehler force f^i given by

$$f^i = \mathbf{n}^i\cdot\left(\hat{\boldsymbol{\sigma}} + \sum_{j\neq i}\boldsymbol{\sigma}^j\right)\cdot\mathbf{b}^i \tag{9}$$

with $\mathbf{n}^i$ the slip plane normal and the Burgers vector $\mathbf{b}^i$ of dislocation i. The direction of this force is in the slip plane and normal to the dislocation line. It is this force that will determine the motion of the dislocation, as will be discussed in the next section.

For edge dislocations with the same magnitude b of the Burgers vector and with $\mathbf{n}^i$ and $\mathbf{b}^i$ parallel to the x_2- and x_1-axes, respectively, the expression for the Peach–Koehler force simplifies to

$$f^i = \sigma^i_{12} b^i. \tag{10}$$

In calculating the Peach–Koehler force, the stress fields due to replicas of each dislocation in the unit cell in all other cells must be accounted for. Even though the self-stress fields decay rapidly with the distance from the dislocation [1, 2], arrays of dislocations have been observed to give rise to very long range effects [e.g. 9 and 15]. In particular, Gulluoglu *et al.* [9] have noted that the truncation of the number of adjacent replicas may give rise to artificial dislocation wall formation. In order to resolve this problem, we developed a procedure in which the summation of fields of any dislocation and all its replicas is split into two steps [8]. First, the summation of the fields is carried out over replicas of each dislocation on the same slip plane. This can be done analytically; the resulting expressions are detailed in Ref. [8] and will not be repeated here. In the second step, the fields due to such infinitely long strings of dislocations are summed over a finite number of replicas of the slip plane above and below the cell. The infinite string solutions decay very rapidly in the normal direction, so that only a few replicas of those strings are needed to obtain accurate results; in the present studies, a total of five replicas were used.

This procedure is adopted for the dislocation stress fields in calculating the Peach–Koehler forces, but also for all other ($\tilde{}$) fields to be substituted in equations (1)–(5). Details are given in Ref. [8]. It is noted that performing the analytical summation over strings of dislocations rather than over walls of dislocations, like in Ref. [9], has the advantage for the present problem that periodicity at the $x_1 = \pm w$ cell faces is realized exactly. This is particularly important for the displacement field $\tilde{\mathbf{u}}$.

2.4. Constitutive relations for motion, creation and annihilation

The magnitude of the glide velocity v^i of dislocation i is taken to be linearly related to the slip plane shear stress through the drag relation

$$\sigma^i_{12} b^i = B v^i \tag{11}$$

where B is the drag coefficient. The value of B is specified relative to the applied shear rate $\dot{\Gamma}$ through the dimensionless number $B\dot{\Gamma}/\mu = 0.38 \times 10^{-11}$ (taking $\mu = 0.26 \times 10^5$ MPa and $B = 10^{-4}$ Pas as representative parameter values for aluminium [11], this corresponds to a shear rate of $\dot{\Gamma} = 10^3\ \mathrm{s}^{-1}$). Because of the periodicity, when the dislocations move, they may leave the cell at $x_1 = \pm w$ but then they re-enter at the opposite side $x_1 = \mp w$.

Obstacles to dislocation motion are modeled as fixed points on a slip plane. Such obstacles account for the effects of small precipitates or for dislocations on other slip systems in blocking slip. However, actually accounting for slip on multiple systems would lead to the obstacle density varying with strain, whereas in the single slip calculations here the density of obstacles remains fixed. Pinned dislocations can only pass the obstacles when their Peach–Koehler force exceeds an obstacle-dependent value. In the calculations here, all obstacles are taken to have the same strength $\tau_{\mathrm{obs}} = 5.7 \times 10^{-3}\,\mu$.

Annihilation of two dislocations with opposite Burgers vector occurs when they are sufficiently close together. This is modeled by eliminating two dislocations when they are within a material-dependent, critical annihilation distance L_e, which is taken to be $L_e = 6b$.

New dislocation pairs are generated by simulating Frank–Read sources. The initial dislocation segment of a Frank–Read source bows out until it produces a new dislocation loop and a replica of itself. The Frank–Read source is modeled in terms of a critical value of the Peach–Koehler force, the time it takes to generate a dislocation loop, and the size of the generated loop. In two dimensions, with single slip, this is simulated by point sources on the slip plane which generate a dislocation dipole when the magnitude of the shear stress at the source, $|\sigma_{12}|$, has exceeded the critical stress τ_{nuc} during a period of time t_{nuc}. The distance L_{nuc} between the dislocations is taken to be specified by

$$L_{\mathrm{nuc}} = \frac{\mu}{2\pi(1-\nu)} \frac{b}{\tau_{\mathrm{nuc}}}. \tag{12}$$

At this distance, the shear stress of one dislocation acting on the other is balanced by the slip plane shear stress. The strength of the dislocation sources is randomly chosen from a Gaussian distribution with mean strength $\bar{\tau}_{\mathrm{nuc}} = 1.9 \times 10^{-3}\,\mu$ and standard deviation of $0.2\bar{\tau}_{\mathrm{nuc}}$. With $\nu = 0.3$, this mean nucleation strength corresponds to a mean nucleation distance of $L_{\mathrm{nuc}} = 125b$. The nucleation time for all sources is taken as $t_{\mathrm{nuc}} = 2.6 \times 10^6\, B/\mu$.

Since no dislocations are present initially and all dislocations are generated in pairs, the net Burgers vector in the material is and remains zero.

3. PARAMETER STUDIES

The studies to be presented here use material parameters that are similar to those in Ref. [8]. The elastic properties of the material system are taken to be given by $\nu = 0.3$, $\nu^* = 0.17$ and $\mu^* = 7.3\,\mu$ (which is representative for an aluminium matrix with silicon-carbide particles). The slip plane spacing in the matrix is $d = 100b$. This value is larger than the

actual slip plane spacing, but is considered representative of the active slip plane spacing. The dimensional characteristics of the microstructure are measured in terms of a material length L which is determined by the Burgers vector, and which is taken as $L = 4000b$. The height of the unit cell for the three morphologies is taken equal to $h = L$, and $w = \sqrt{3}h \approx 1.73h$ in all cases as shown in Fig. 2 (with $b = 2.5 \times 10^{-10}$ m, the Burgers vector for copper as a representative parameter value, the length $L = 1$ μm so that the cell has dimensions 3.46 μm by 2 μm); one calculation is repeated with $h = L/2$, keeping $w = 1.73h$.

3.1. *Morphologies*

Three reinforcement morphologies are considered. Two have square particles with different area fractions $f = (2w_f h_f)/(wh)$, while the third morphology has particles having aspect ratio two. The geometric parameters characterizing these reinforcement morphologies are:

(i) square particles ($h_f = w_f$) with an area fraction $f = 0.2$, i.e. $h_f = 0.416h$;
(ii) square particles ($h_f = w_f$) with an area fraction $f = 0.289$, i.e. $h_f = 0.5h$;
(iii) particles with $h_f = 2w_f$ with an area fraction $f = 0.2$, i.e. $h_f = 0.588h$.

Morphology (i) has the same area fraction of reinforcing particles as used in Ref. [8] but now arranged in a hexagonal packing rather than in a cubic array. This morphology implies layers of strings of particles which are separated by unreinforced veins of matrix material having height $h - 2h_f = 0.168h$. It was found for the cubic packing in Ref. [8], and will be seen subsequently for the hexagonal packing, that dislocation activity tends to concentrate in these matrix veins. Therefore, morphology (ii) is designed with all slip planes ending at an interface with a particle so that the veins have zero thickness. The third morphology has the same area fraction as (i) but, because of their oblate shapes, the particles do not leave any unreinforced veins of matrix material.

For each of these particle morphologies, dislocation sources and obstacles were generated at random, but with approximately the same densities: (i) $\rho_{nuc} = \rho_{obs} = 61.2L^{-2}$; (ii) $\rho_{nuc} = \rho_{obs} = 46.2L^{-2}$; (iii) $\rho_{nuc} = \rho_{obs} = 55.4L^{-2}$. Here, and subsequently, densities are measured per unit of total area (normalized by the material length scale L for convenience), including particles; densities per unit matrix area are readily obtained by dividing by $1 - f$. The precise locations of sources and obstacles will be shown in the upcoming figures. In all cases, the matrix is taken to be dislocation free initially. As the shear strain is increased, dislocation dipoles will be generated, dislocations will move and possibly get pinned at obstacles or at the matrix–particle interface.

Figure 3(a) shows the overall shear stress response to the applied simple shear for each of the three materials (the shear stress $\bar{\tau}$ is normalized by the matrix shear modulus μ). The serrations on the stress–strain curve, which are associated with discrete dislocation events, are so prominent because of the limited number of dislocations in a unit cell. The corresponding evolution of the dislocation density is depicted in Fig. 3(b) with the mobile dislocations monitored separately. The differences in response among the different materials become most clear when also looking at the dislocation distributions. These are shown for each of the materials in Figs 4–6, respectively, at two strain levels. Also shown, in parts (a) of these figures, are the distributions of sources and obstacles.

In material (i), the first dislocations are generated in the veins between the strings of particles. As these dislocations glide, they generate new dislocations on the same or on neighboring slip planes. Since the motion of these dislocations is not blocked by particles, this leads to progressive concentration of all dislocation activity into one of the veins in the cell [see Fig. 4(a), (b)] at rather small strains. The shear stress–shear strain response in Fig. 3(a) exhibits a peak or "yield" stress associated with the generation of a sufficient number of mobile dislocations, followed by a plateau or "flow" stress associated with localization of dislocation activity. This flow stress

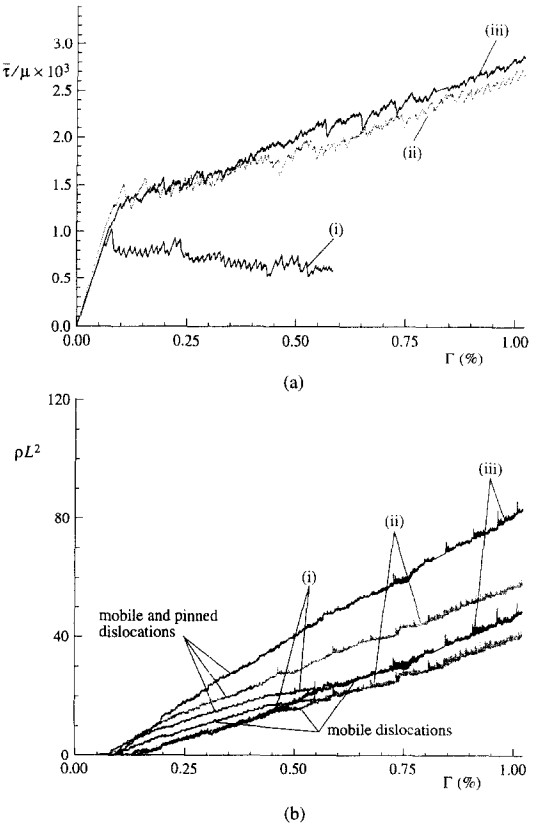

Fig. 3. Effect of morphology on (a) overall shear stress response and (b) evolution of dislocation density. Dislocation distributions in materials (i)–(iii) are shown in Figs 4–6.

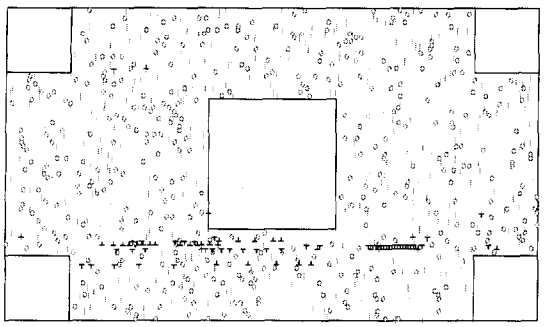

(a)

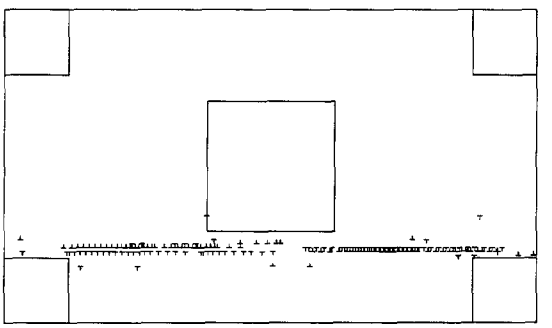

(b)

Fig. 4. Dislocation distributions in material (i) at (a) $\Gamma = 0.25\%$, (b) $\Gamma = 0.58\%$. The distribution of sources (grey ○) and obstacles (grey |) is shown in (a).

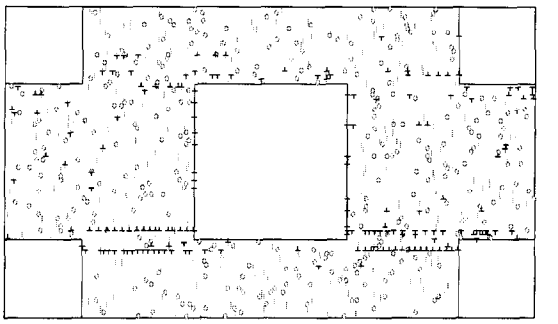

(a)

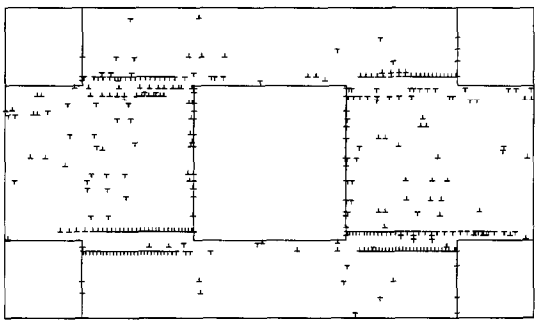

(b)

Fig. 5. Dislocation distributions in material (ii) at (a) $\Gamma = 0.46\%$, (b) $\Gamma = 1.0\%$. The grey ○ and | in (a) indicate the sources and obstacles, respectively.

slowly drops with increasing strain as the density of dislocations gradually increases, until at $\Gamma \approx 0.5\%$ a steady state is attained with a constant dislocation density [see Fig. 3(b)].

In material (ii) the square particles are just large enough to block all slip planes. Nevertheless, a strong effect is seen in the fact that the top of the central particle lines up with the bottom of the upper particles, and similarly for the bottom face of the particle. This leads to substantial concentration of dislocation activity on the slip planes directly next to the particle top and bottom [see Fig. 5(a)]. Many of these dislocations get trapped in pile-ups against a particle interface, leading to strong stress fields that generate dislocations elsewhere in the material, giving rise to several dislocations piling up against the sides of the particles [see Fig. 5(b)]. As a consequence, the total dislocation density increases more rapidly than in material (i), whereas the density of mobile dislocations remains somewhat lower. The density of immobile dislocations continues to increase with ongoing deformation, and the material exhibits almost linear hardening (see Fig. 3).

The generation of dislocations in material (iii) is still more uniform than in material (ii) (see Fig. 6), because of the complete absence of veins of unreinforced matrix. Also, much stronger piling-up against the particle sides is observed, especially at the larger strain level shown in Fig. 6(b). The density of

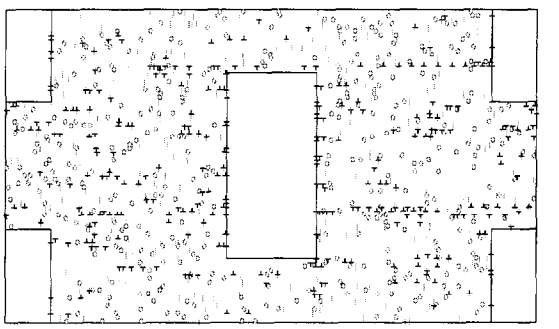

(a)

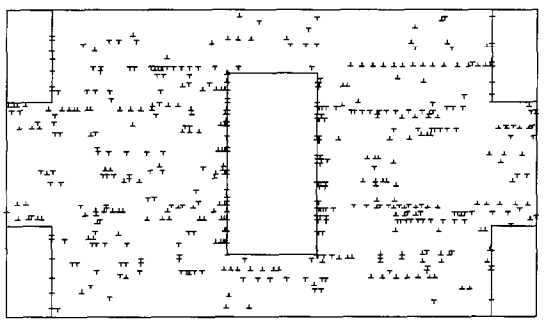

(b)

Fig. 6. Dislocation distributions in material (iii) at (a) $\Gamma = 0.58\%$, (b) $\Gamma = 0.96\%$. The grey ○ and | in (a) indicate the sources and obstacles, respectively.

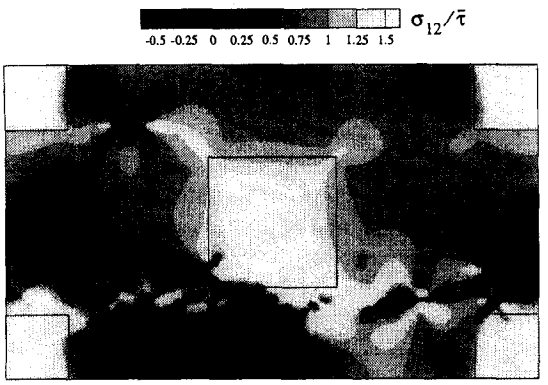

Fig. 7. Shear stress distributions, normalized by the current overall shear stress $\bar{\tau}$, in material (i) at (a) $\Gamma = 0.25\%$, (b) $\Gamma = 0.58\%$ (see Fig. 4).

mobile dislocations is slightly larger than in material (ii), but the immobile dislocation density is significantly larger for this morphology (see Fig. 3). The fact that the stress–strain curves for materials (ii) and (iii) differ very little is evidence for hardening not being determined merely by dislocation density or area fraction of reinforcing particles but also by the reinforcement morphology.

At each stage of the deformation, the stress field in the material is known. The distributions of the total shear stress σ_{12} for morphologies (i) and (iii) are shown in Figs 7 and 8 at the same stages of deformation as in the previous dislocation distribution plots. The contour levels in each of the figures is chosen so as to focus on the stress fields in the matrix; stress distributions inside the particles will be presented later on. Especially for morphology (i) with relatively low dislocation densities, as in Fig. 7, the stress peaks of the individual dislocations are clearly visible as well as the long-range effect of the fields. In the neighborhood of the particles, there are substantial regions in the matrix where the shear stresses are a factor of two or more larger (or smaller) than the average shear stress. In materials (ii) and (iii) the dislocation density becomes substantially larger. As a consequence, the stress distribution becomes more and more jagged with increasing strain, as seen in Fig. 8 for material (iii). At the same time, the regions of predominantly larger (or smaller) than average stresses become smaller. The zones of very high positive shear stress in the matrix on either side of the central particle appear to be exceptions; their size does not change much even though the dislocation density has almost doubled. It should be noted that in regions of high dislocation density, the plots may not fully reflect the singularities associated with individual dislocations†.

As expected on the basis of the dislocation distributions seen in Figs 4–6, the total displacement fields are highly non-uniform over the material. This is illustrated very clearly in the deformed meshes shown in Fig. 9 for each of the three morphologies at the largest strain level presented before. For both materials (i) and (ii) the applied macroscopic shear is accommodated in one or a few bands of intense shearing located near the top or bottom faces of the central particle. In material (iii), shown in Fig. 9(c),

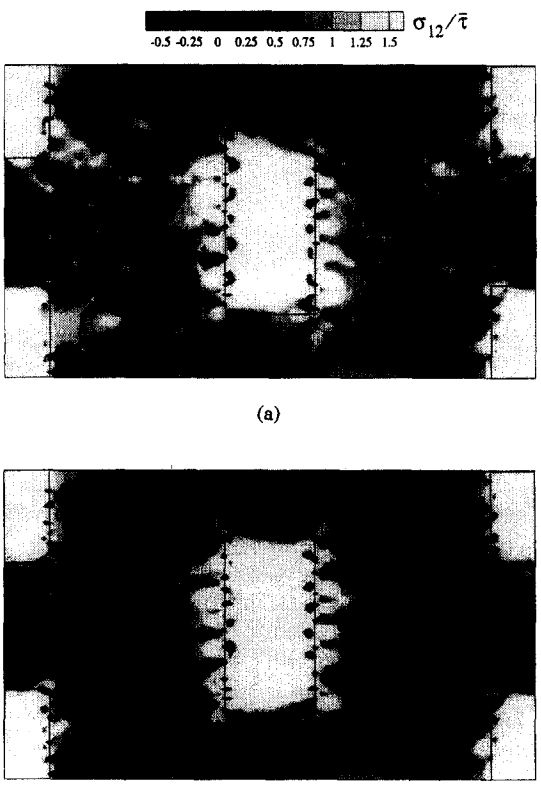

Fig. 8. Shear stress distributions, normalized by the current overall shear stress $\bar{\tau}$, in material (iii) at (a) $\Gamma = 0.58\%$, (b) $\Gamma = 0.96\%$ (see Fig. 6).

†The dislocation contribution $\tilde{\sigma}_{12}$ to the stresses in Figs 7 and 8 and in subsequent stress contour plots is based on the values at the four integration points of the finite element mesh. These values and the integration point values of $\hat{\sigma}_{12}$ are then extrapolated to the nodal points for plotting. The plots are produced by the commercial software Tecplot from Amtek Engineering Inc., Bellevue, WA.

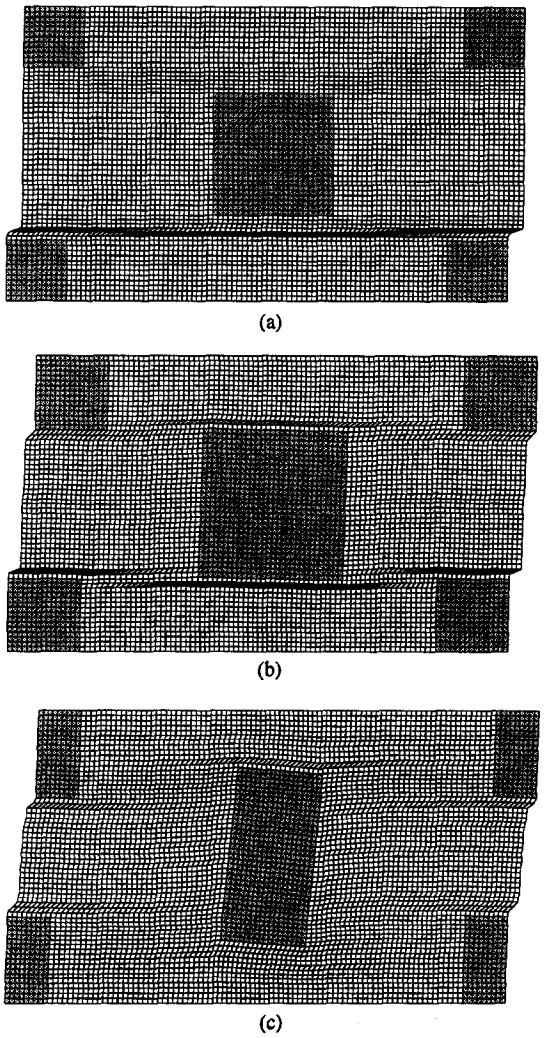

Fig. 9. Deformed meshes for (a) material (i) at $\Gamma = 0.58\%$, (b) material (ii) at $\Gamma = 1.0\%$, (c) material (iii) at $\Gamma = 0.96\%$. All displacements are magnified by a factor of 10. The shaded areas represent the particles.

the displacements are more uniformly distributed. This then leads to substantial rotation of the central particle in the shearing direction, and significant curvature of the mesh lines.

3.2. *Dislocation sources and obstacles*

In addition to material parameters, the results presented in the previous section depend on the distributions of sources and obstacles that are assumed. To get some feeling for the sensitivity of the results to these distributions, the computation for morphology (iii) has been repeated for a different realization of the source and obstacle distributions with the same respective densities as before. Otherwise, all parameters are left unchanged.

Comparing the results in Fig. 10 with corresponding results for the first realization shown in Fig. 3, we see that the overall stress–strain responses are virtually the same, even though the total dislocation density for the second realization lags behind that of the first realization by about 10%. Consistent with this, the densities of mobile dislocations evolve in much the same way.

Evidently, the distribution of dislocations at any instant differs from that obtained with the first realization. This is illustrated in Fig. 11(a) showing the distribution at about the same strain as that in Fig. 6(a) for the first realization. Hence, the precise stress distributions in the two realizations will also differ, as we see by comparing the shear stress distribution shown in Fig. 11(b) with that found at about the same strain for the first realization [see Fig. 8(a)]. However, the two distributions do share a number of characteristics, such as the average mean spacing between stress peaks (related to the current dislocation density), the zones of high shear stresses on the left- and right-hand sides of the central particle, and the shielding above and below the central particle. From the deformed mesh shown in Fig. 11(c) we observe that the bands of concentrated shearing do not occur at the same locations and do not have the same dimensions as those found in Fig. 9(c) for the first realization [note that the strain in Fig. 9(c) is nearly twice that in Fig. 11(c)], although the bands do have the same tendency to form

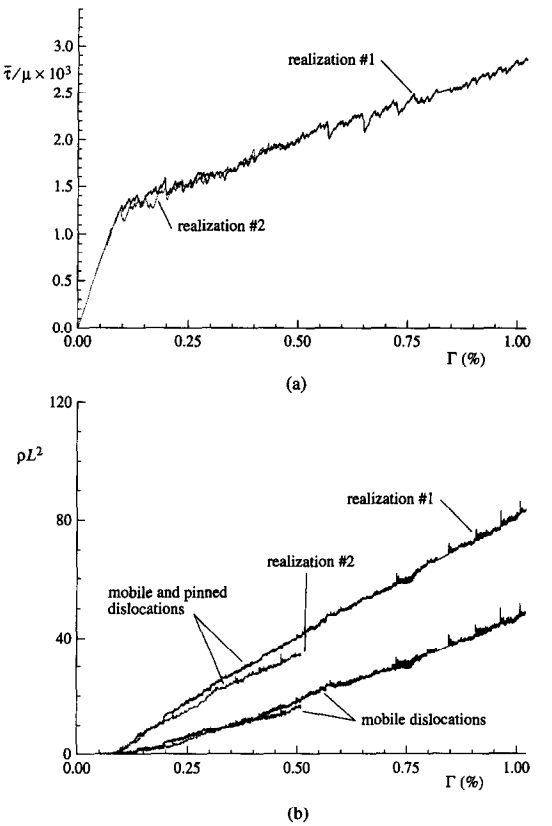

Fig. 10. Effect of distributions of sources and obstacles in material (iii) on (a) overall shear stress response and (b) evolution of dislocation density. The first realization corresponds to the results shown previously in Figs 3 and 6. The distributions of source and obstacles for the second realization are shown in Fig. 11(a).

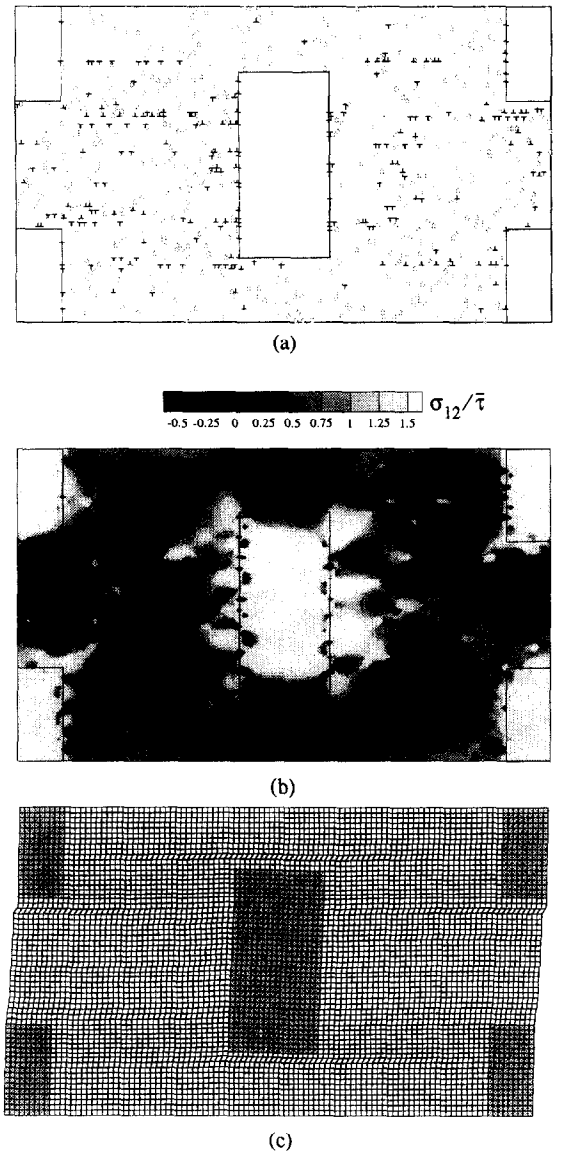

Fig. 11. Results at $\Gamma = 0.51\%$ for the second realization of source and obstacle distributions in material (iii): (a) dislocation distributions (including source and obstacle distributions); (b) shear stress distribution, normalized by the current overall shear stress $\bar{\tau}$; (c) deformed mesh (displacements magnified by a factor of 10). The overall response is shown in Fig. 10.

preferentially above and below the particles in the cell. Thus, even though the local details differ, the two realizations of material (iii) give essentially the same stress–strain response over the range calculated.

3.3. *Reinforcement size*

For morphology (iii), we analyze the effect of the size of the particles by reducing their size and the size of the cell by a factor of two, so that the area fraction occupied by the particles remains unchanged. In this case, $h = L/2$ instead of $h = L$ as in all previous cases. The applied velocity is halved so that the macroscopic shear rate is the same as before. The density of sources and obstacles is taken to be the same as before for material (iii). The actual distributions of obstacles and sources are obtained from the case with the original size particles shown in Fig. 3(a) by removing every second slip plane and every second source or obstacle on the remaining slip planes.

According to Fig. 12(a), the stress–strain response for the material with smaller particles differs from the one with the larger particles in two respects. First, and most importantly, the overall hardening rate is higher for the material with the smaller particles: $0.19\ \mu$ vs $0.16\ \mu$ for the twice larger particles. This is in line with the finding in Fig. 12(b) that the density of immobilized dislocations is consistently larger. Second, the response is more serrated: the stress drops, associated with the nucleation of new dislocation pairs, are more pronounced. This is attributed to the fact that we are dealing with a doubly-periodic array of cells, so that each nucleation event is taking place simultaneously at all other replicas; the material with the smaller particles ($h = L/2$) has four times more replicas per unit area.

Figure 13(a) shows the distribution of dislocations in this material at the same strain level as in Fig. 6(b)

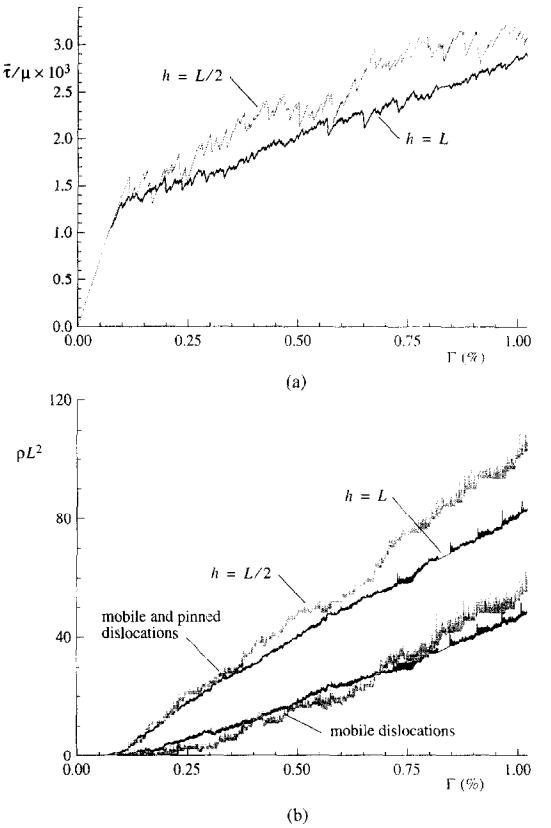

Fig. 12. Effects of the particle size in material (iii) on (a) overall shear stress response, and (b) evolution of dislocation density. The results for the larger particles ($h = L$) have been shown previously in Fig. 3. The distributions of source, obstacles and dislocations for the case with the smaller particles ($h = L/2$) are shown in Fig. 13(a).

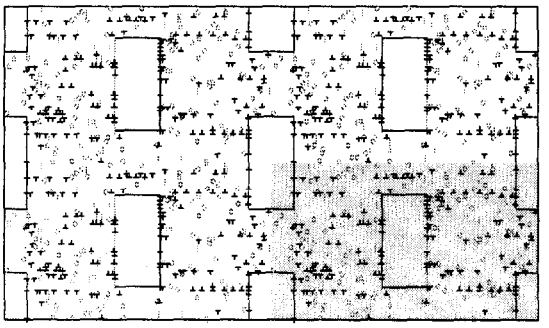

(a)

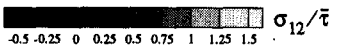

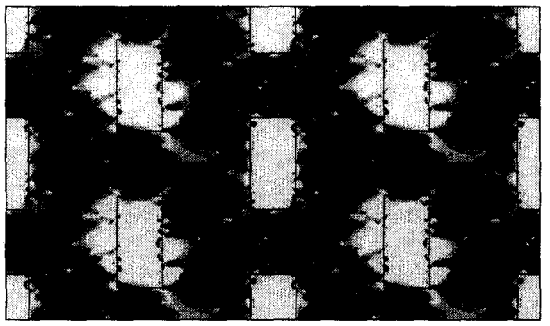

(b)

(c)

Fig. 13. Results at $\Gamma = 0.96\%$ for the material with morphology (iii) but with half-size particles ($h = L/2$): (a) dislocation distribution (including source and obstacle distributions); (b) shear stress distribution, normalized by the current overall shear stress $\bar{\tau}$; (c) deformed mesh (displacements magnified by a factor of 10). The overall response is shown in Fig. 12. To simplify comparison with previous results for $h = L$, four replicas of the unit cell are shown.

for the material with $h = L$. For a proper comparison, a total of four replicas is shown in this figure so that the region shown has the same physical dimensions as in Fig. 6. Clearly, even though the dislocation densities do not differ much, the distributions around the particles differ greatly from the previous cases. The influence that this has on the stress distributions inside the material is shown in Fig. 13(b). When comparing this shear stress distribution with the corresponding one in Fig. 8(b) for the original, larger particles, one observes that the regions of high shear stresses adjacent to the particles do not scale with the particle size. In fact, these regions are approximately the same size for both cases. This is part of the explanation for the higher strain hardening in the material with the smaller reinforcing particles. The displacement fields inside each unit cell, shown again by a deformed mesh in Fig. 13(c), have essentially the same features of localization as for the case with larger particles (see Fig. 9). It should be noted that this plot of four replicas of the cell clearly brings out the fact that the fields around the particles located in the center of each cell are different from those around particles that are in the corners of the cell; this is a direct consequence of the way boundary conditions are prescribed.

4. COMPARISON WITH CONTINUUM SLIP THEORY

4.1. *Continuum slip theory*

For comparison purposes, calculations are carried out for the plane strain unit cell in Fig. 2 using continuum slip plasticity to describe the material response. Overviews of the continuum slip formulation and its physical background are given in Refs [3–5]. In order to facilitate a direct comparison with the dislocation results, a small displacement gradient formulation is used.

As mentioned before, the material is taken to have one slip system, with the slip plane normal $\mathbf{n}$ parallel to the x_2-axis and with the slip direction $\mathbf{m}$ parallel to the x_1-axis. The total strain rate $\dot{\epsilon}$ is written as the sum

$$\dot{\epsilon} = \dot{\epsilon}^e + \dot{\epsilon}^p \tag{13}$$

where the elastic strain rate $\dot{\epsilon}^e$ is given in terms of the stress rate $\dot{\sigma}$ by Hooke's law

$$\dot{\epsilon}^e = \mathscr{L}^{-1}:\dot{\sigma} \tag{14}$$

and the plastic strain rate $\dot{\epsilon}^p$ is given by

$$\dot{\epsilon}^p = \frac{\dot{\gamma}}{2}(\mathbf{m} \otimes \mathbf{n} + \mathbf{n} \otimes \mathbf{m}). \tag{15}$$

Combining equations (13), (14) and (15), and inverting to obtain the stress rate–strain rate relation gives

$$\dot{\sigma} = \mathscr{L}:\left[\dot{\epsilon} - \frac{\dot{\gamma}}{2}(\mathbf{m} \otimes \mathbf{n} + \mathbf{n} \otimes \mathbf{m})\right]. \tag{16}$$

The material is taken to be viscoplastic, with the strain rate given by the power law relation

$$\dot{\gamma} = \dot{a}\left(\frac{\tau}{g}\right)\left(\left|\frac{\tau}{g}\right|\right)^{(1/m)-1}. \tag{17}$$

Here, $\dot{a}$ is a reference strain rate, m is the strain rate hardening exponent, g is the slip system hardness, and the slip system resolved shear stress, τ, is σ_{12}. In

all calculations here, $\dot{a}/\dot{\Gamma} = 0.5$ and $m = 0.005$. The slip system strain hardening is described by

$$g(\gamma) = \tau_0 + \frac{\gamma_0 h_0}{N}\left[\left(\frac{\gamma}{\gamma_0} + 1\right)^N - 1\right], \qquad (18)$$

where τ_0 is the slip system strength, γ_0 is a reference strain, h_0 is the initial hardening rate and N is the strain hardening exponent.

The finite element formulation used in conjunction with this theory is based on the rate principle of virtual work

$$\int_V \dot{\sigma}:\delta\dot{\epsilon}\, dV = \int_{S_f} \dot{\mathbf{T}}_0 \cdot \delta\dot{\mathbf{u}}\, dS. \qquad (19)$$

The finite element discretization is based on quadrilateral elements consisting of four "crossed" linear displacement triangles. The same 102×60 quadrilateral mesh is used as in the discrete dislocation calculations. The unit cell is subject to the boundary conditions (7) together with periodicity at $x_1 = \pm w$, and the deformation history is calculated in a linear incremental manner. In order to increase the stable time step, the rate tangent modulus method in Ref. [6] is used for the time integration.

4.2. *Dislocation vs continuum slip predictions*

In order to make a comparison between the fields according to the discrete dislocation model and the continuum slip model, the yield stress τ_0 and the hardening parameters γ_0, h_0, and N are fitted by a trial and error process of assuming matrix yield stress and strain hardening parameter values, calculating the composite response, and then adjusting the strain hardening parameter values to improve the agreement with the dislocation model computations. We obtain $\gamma_0 = 0.01$, $N = 0.1$, $(\gamma_0 h_0)/(N\tau_0) = 1.43$, and $\tau_0/\mu = 5.3 \times 10^{-4}$ for material (i); $\gamma_0 = 0.002$, $N = 1.0$, $(\gamma_0 h_0)/(N\tau_0) = 1.76 \times 10^{-2}$, and $\tau_0/\mu = 1.12 \times 10^{-3}$ for material (ii); and $\gamma_0 = 0.002$, $N = 1.0$, $(\gamma_0 h_0)/(N\tau_0) = 3.77 \times 10^{-2}$, and $\tau_0/\mu = 1.31 \times 10^{-3}$ for material (iii). All three of these characterizations give rise to very little strain hardening in the unreinforced matrix material for shear strains of up to 1%.

Figure 14 shows the composite shear stress (normalized by the matrix shear modulus μ) vs shear strain curves computed using these three sets of material parameters together with the discrete dislocation curves from Fig. 3(a). Although the reinforcement area fractions for materials (ii) and (iii) differ ($f = 0.20$ and $f = 0.289$, respectively) and the matrix hardening rates differ, their combined effect is to give very similar composite strain hardening rates. As seen in Fig. 14 the fits give only an approximate agreement, because the form (18) is not sufficiently general to describe the response over the entire strain range and because of the strongly serrated dislocation-based response. In particular, note that material (i) exhibits strain softening over a range of shear strain before the shear stress reaches a more or less constant steady state value, while for the continuum a monotonic strain hardening relation is used. However, an approximate fit suffices for the present purpose. The composite shear stress vs shear strain curve predicted by continuum slip theory for material (i) differs only slightly from the unreinforced matrix shear stress vs shear strain curve, whereas those for materials (ii) and (iii) show substantial composite hardening.

Figure 15 depicts the shear stress fields as obtained from the continuum slip calculations for morphologies (i) and (iii). The strain levels correspond to those in Figs 7(b) and 8(b) for the dislocation plasticity results. A comparison of these two sets of figures immediately shows that the stress distributions according to the continuum slip model are very different from those found using the discrete dislocation model. The main reason for this difference is that the singular stress field of each individual dislocation appears in Figs 7 and 8. Furthermore, in the continuum slip results, the regions of relatively high stress in the matrix are regions of relatively large plastic flow where substantial strain hardening has taken place. This is most clearly seen in the veins between particles for morphology (i) in Fig. 15(a). Thus, the continuum-based stress distributions are to an important extent determined by plastic flow being non-uniform in the matrix but not highly localized. This is notably different from the discrete dislocation-based stress fields.

What the stress distributions in Fig. 15 also show is that the shear stresses inside the particles in morphology (i) are substantially smaller than in morphology (iii). However, the scaling in these figures has been chosen to highlight the matrix stress fields, and is not suitable for studying the particle stress distributions. Therefore, Fig. 16 separately shows the shear stress distributions inside the particles for all three morphologies, both according

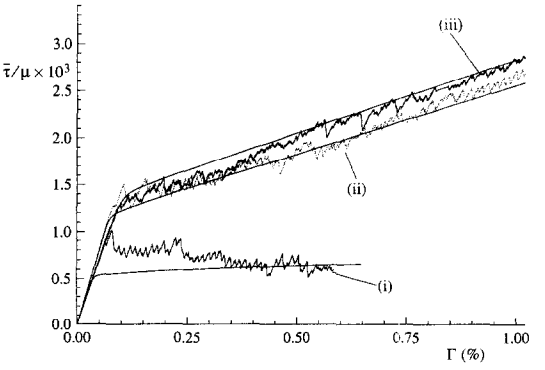

Fig. 14. Overall shear stress response in materials (i)–(iii) according to the dislocation plasticity model, as shown previously in Fig. 3, and according to the continuum slip description using the values of the hardening parameters indicated in the text.

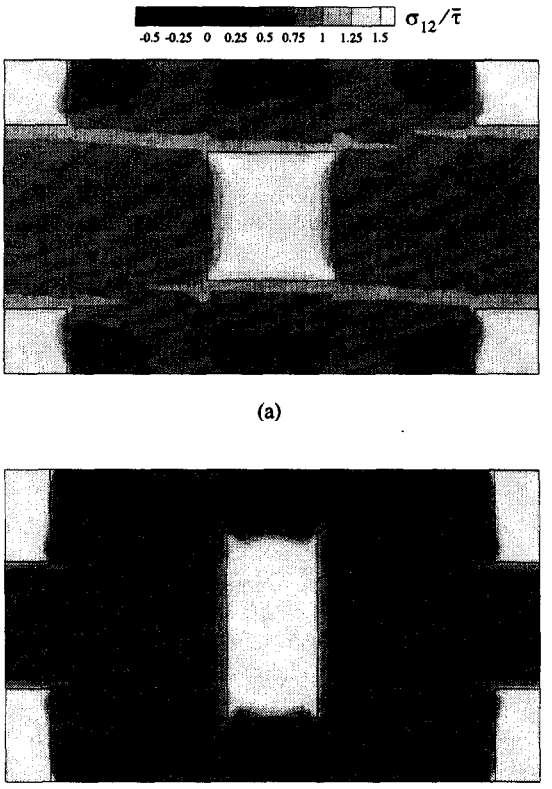

Fig. 15. Shear stress distributions obtained from the continuum slip modeling in (a) material (i) at $\Gamma = 0.58\%$, (b) material (iii) at $\Gamma = 0.96\%$. In each case, the stresses are normalized by the corresponding current overall shear stress $\bar{\tau}$.

to the discrete dislocation and the continuum slip models. For each of the morphologies it is possible to discover common features in the stress distributions according to the two descriptions, but the dislocation-based stress distributions clearly show the localized stress peaks that are due to nearby matrix dislocations. Each such peak not only reflects the direct, infinite body field of the dislocation, as given by the ($\tilde{}$) fields, but also the interaction stress field with the particle through the ($\hat{}$) fields [see equations (1) and (4)]. Moreover, for morphology (ii) and even more so for morphology (iii) the shear stress in the central region of the particle appears to be higher for the dislocation-based results than in the continuum slip model. This is, at least in part, caused by the long-range stress fields of the many dislocations that have piled up against the particle in those cases. The above observations suggest that there may be a significant difference in the average values of the shear stress over the entire particle as predicted by the two descriptions. To explore this further, Table 1 lists the shear stress averages (denoted by $\langle\cdot\rangle$) over the two phases for each case. The values in the last two columns must, of course, satisfy

$$f\langle\sigma_{12}\rangle^{*} + (1-f)\langle\sigma_{12}\rangle^{M} = \bar{\tau} \qquad (20)$$

where the superscript * refers to the particle phase and M to the matrix phase.

The average shear stress $\langle\sigma_{12}\rangle^{*}$, relative to the overall average shear stress $\bar{\tau}$, in the particle for all discrete dislocation analyses is higher than predicted by the continuum model. As an immediate consequence, the average over the matrix for the dislocation results is in all cases lower than the continuum slip prediction. Furthermore, the case with smaller particles, $h = L/2$, is seen to give rise to the largest average stress in the particle, thus giving further evidence for a size effect when using the dislocation description. It must be noted, however, that the results for the two realizations of material (iii) with $h = L$ show that there is a dependence on the source and obstacle distributions, so that care must be taken in generalizing this size effect.

4.3. *Averages of stress fields*

Having seen the large differences in stress fields according to the dislocation plasticity model in comparison with a continuum-based description, the question arises as to whether, and how, the continuum limit is approached. In this section we address this question by considering averages of the shear stress fields over windows of various sizes. The

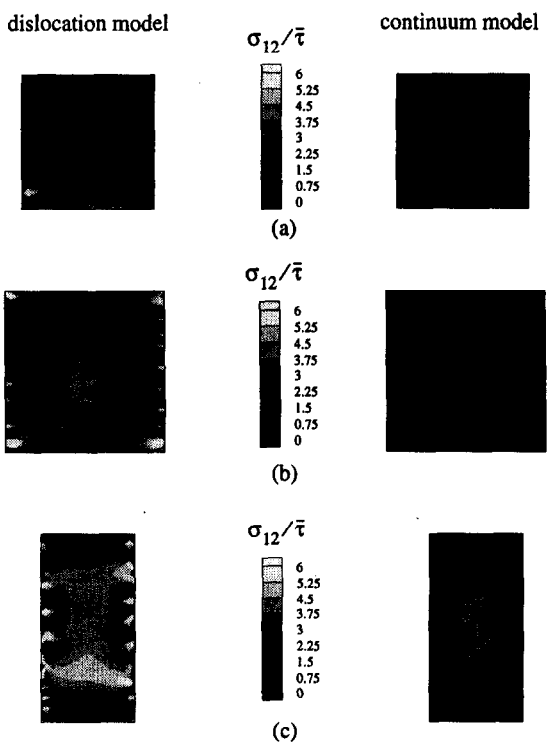

Fig. 16. Shear stress distributions inside the particles for (a) material (i) at $\Gamma = 0.58\%$, (b) material (ii) at $\Gamma = 1.0\%$, (c) material (iii) at $\Gamma = 0.96\%$. Results according to the discrete dislocation modeling are on the left-hand side [cf. Figs 7 and 8 for materials (i) and (iii)] and those based on the continuum slip formulation on the right-hand side (cf. Fig. 15). In each case, the stresses are normalized by the corresponding current overall shear stress $\bar{\tau}$.

Table 1. Phase average shear stresses for the three morphologies based on the dislocation plasticity results (dislocation) or on the continuum slip results (continuum). The labels #1 and #2 indicate the two cases with different realizations of sources and obstacles; the label 1/2 indicates the case with the smaller particles ($h = L/2$ instead of $h = L$)

		$\langle\sigma_{12}\rangle/\mu \times 10^3$			$\langle\sigma_{12}\rangle/\bar{\tau}$	
Material	Γ (%)	Cell	Matrix (M)	Particle (*)	Matrix (M)	Particle (*)
(i) dislocation	0.58	0.57	0.43	1.15	0.749	2.00
(i) continuum	0.58	0.65	0.54	1.08	0.833	1.67
(ii) dislocation	0.46	1.58	0.69	3.77	0.437	2.39
(ii) continuum	0.46	1.77	1.13	3.34	0.638	1.89
(iii) (#1) dislocation	0.58	1.98	0.96	6.04	0.484	3.06
(iii) (#2) dislocation	0.51	1.95	1.02	5.64	0.524	2.90
(iii) (1/2) dislocation	0.58	2.45	1.26	7.21	0.513	2.94
(iii) continuum	0.58	2.18	1.43	5.14	0.658	2.36

size of a window is denoted by A_w and the corresponding average is

$$\langle\sigma_{12}\rangle = \int_{A_w} \sigma_{12}\, dx_1\, dx_2. \tag{21}$$

For brevity, we confine attention to results for morphology (iii).

The largest relevant window is equal to the unit cell, and the average of the shear stress field over this window is equal to the applied shear stress $\bar{\tau}$. Upon systematically reducing the size of the windows, the next smallest set of windows would be one window covering the matrix and a window over the particles in the cell. Averages over these windows have already been considered in the previous section. Figure 17 illustrates the procedure we have adopted to gradually refine the window size over the matrix. The subdivision of the matrix region is designed so that for each number of windows per cell matrix as indicated in Fig. 17 the sizes of the individual windows are close to their average size.

The bar charts depicted in Figs 18 and 19 give a summary of the window-average shear stresses for the three realizations of morphology (iii). The bar charts are produced by computing the minimum and maximum value of $\langle\sigma_{12}\rangle$ for each of the window sizes in Fig. 17, and plotting these values in a bar against A_w/A_m. Thus, these plots show how the range of values $\langle\sigma_{12}\rangle$ gradually shrinks as the area over which

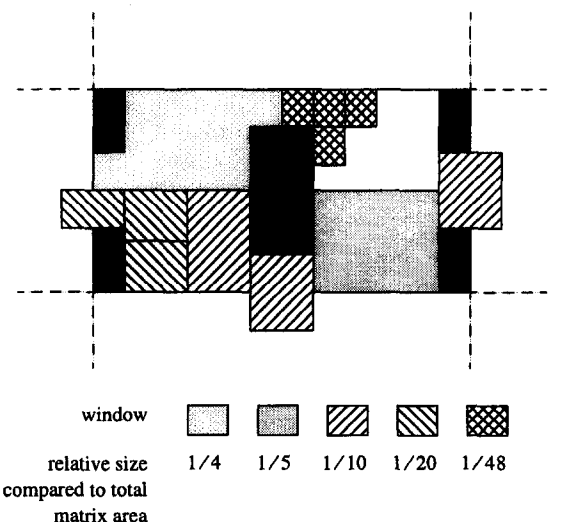

Fig. 17. Definition of the windows within the matrix of morphology (iii) for various average window sizes, giving a total 4, 5, 10, 20 or 48 windows in the matrix.

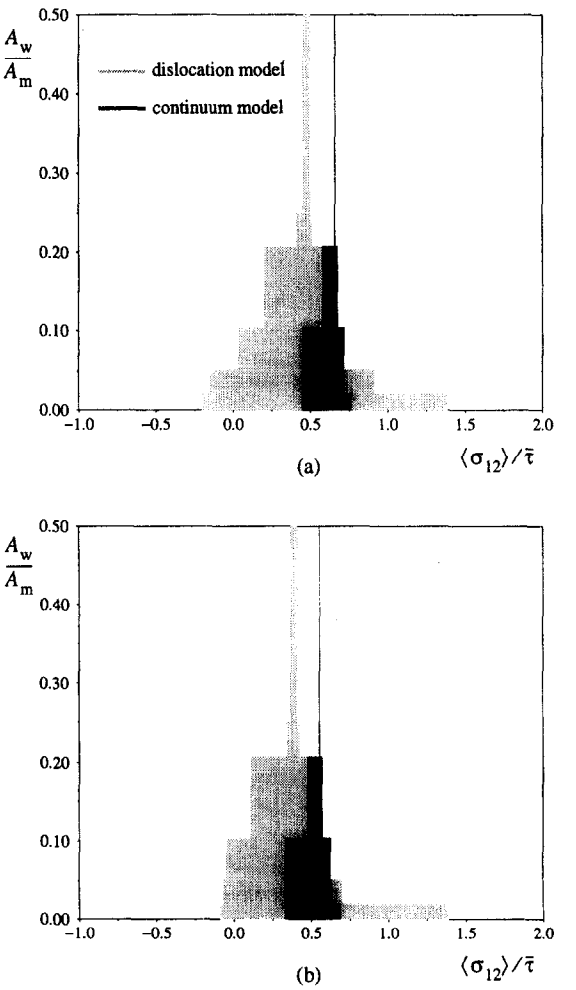

Fig. 18. Bar chart of window-averaged shear stresses in the matrix for morphology (iii) at (a) $\Gamma = 0.58\%$, (b) $\Gamma = 0.96\%$. The dislocation model results are based on the case shown in Fig. 8, and the continuum results are from Fig. 15(b).

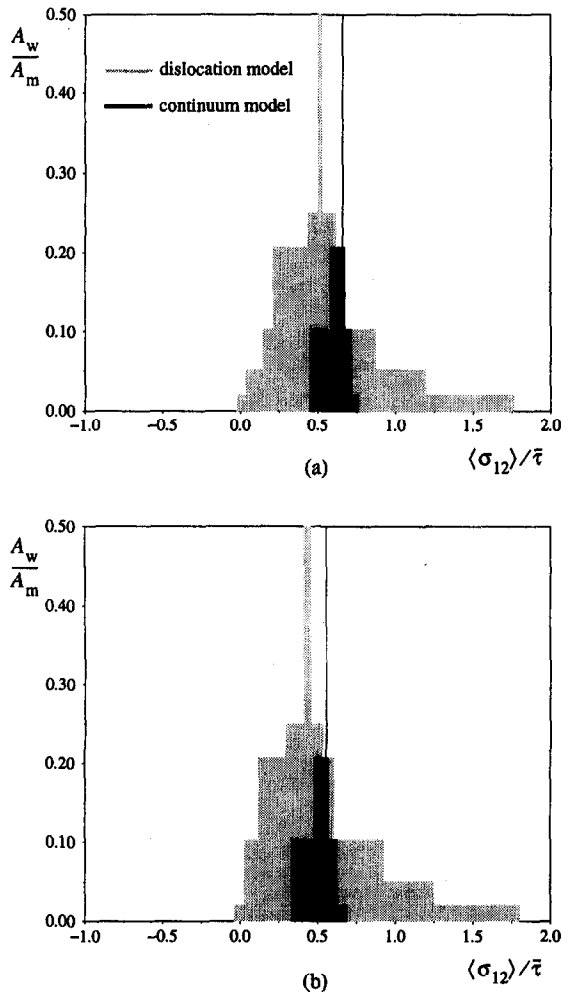

Fig. 19. Bar chart of window-averaged shear stresses in the matrix for morphology (iii) with the smaller particles, $h = L/2$, at (a) $\Gamma = 0.58\%$, (b) $\Gamma = 0.96\%$ [see Fig. 13(b)].

it is averaged is increased. There are two main differences in the bar charts thus obtained on the basis of the dislocation model results and the continuum results. First, the location of the peaks is different; these peaks correspond to the average values for the entire matrix, and we have already seen in Table 1 that the continuum model systematically yields higher values than the dislocation model. Second, the dislocation-based bar charts are much wider than those for the continuum model. This is due to the fact that as the window size decreases, the singular stress fields of the individual dislocations in any window no longer cancel; in the limit of vanishingly small windows one of course recovers all singularities and stresses range from $-\infty$ to $+\infty$. In Fig. 18, we observe that the width of the dislocation-based bar chart reduces somewhat with increasing strain and increasing dislocation density. But it is not clear if this is a systematic tendency, since the bar chart for the dislocation model result with the second realization of sources and obstacles (not shown) exhibits a similar difference in shape from the one in Fig. 18(a). Comparing the bar charts for the case with smaller particles shown in Fig. 19 with those in Fig. 18, it is seen that the distribution of average stresses is somewhat wider for the smaller particles, which is indicative of a size effect.

5. DISCUSSION

Although the model is highly idealized, the results exhibit characteristic features of plastic flow in two-phase materials. For example, the deformation fields have regions of highly localized deformation [Figs 9, 11(c), and 13(c)]; the effective matrix flow properties depend on the reinforcement morphology (Fig. 14); and the composite stress–strain response depends on particle size (Fig. 12). In this regard, it is worth emphasizing that the stress–strain response of the matrix is an outcome in the discrete dislocation calculation, whereas it is an input for a continuum analysis.

Three particle morphologies were analyzed. For material (i), where there is a vein of unreinforced matrix material (Fig. 4), the overall stress–strain response is essentially that of the unreinforced material, as also found in Ref. [8]. Additionally, a more or less constant flow stress is reached, i.e. a stage I type stress–strain response, with shearing localized on one or a few of the unblocked matrix slip planes. On the other hand, for materials (ii) and (iii), the reinforcements block every slip plane. For these materials, the stage I type response is absent. After yield, the average slope of the stress–strain curves for materials (ii) and (iii) in Figs 3(a), 10(a) and 12(a) is nearly constant. The resulting hardening modulus is $\approx 0.19\,\mu$–$0.16\,\mu$ (depending on particle size), which is a reasonable range for an aluminium matrix reinforced with hard particles (see, for example, Fig. 14 in Ref. [18]).

Regardless of the reinforcement morphology, the discrete dislocation results show regions of highly localized deformation (Fig. 9) that arise as a consequence of localized dislocation activity on one or a few slip systems. Since the highly localized deformations are associated with the discrete dislocations, which are represented analytically, the fact that these deformation fields are concentrated in a row of elements does not indicate a mesh dependence of the results (such a mesh dependence would be the case for localized deformations in a rate-independent strain softening continuum); it is simply an indication of how highly localized the displacement fields are for a row of discrete dislocations. If a strain softening slip system relation had been used for material (i) instead of the hardening relation (18), localization of deformation into a narrow band would have occurred in that continuum slip calculation due to a material instability. However, it is worth noting that for materials (ii) and (iii), the highly localized deformations develop while the overall shear stress

continues to increase. The response for materials (ii) and (iii) is quite different from what would occur for localizations associated with a material instability.

For materials (ii) and (iii), which both exhibit significant hardening, shearing necessarily involves rotation of the central particle in the cell. Dislocations pile up at the particle sides (Figs 5 and 6), forming dislocation walls or tilt boundaries. These dislocations are "geometrically necessary" to accommodate the particle rotation. Indeed, a two-phase material like the one analyzed here was specifically considered by Ashby [16] in elucidating the concept of geometrically necessary dislocations. In Ashby's description, the density of geometrically necessary dislocations increases linearly with strain, while, in addition, statistically stored dislocations are being generated during the deformation process. Figure 3 shows that the total dislocation density increases linearly with strain. Closer examination of the actual dislocation distributions, as in Fig. 6, reveals that the fraction of geometrically necessary dislocations is roughly constant (and equal to $\approx 1/3$) in the strain range here, so that in our analyses an outcome is that their density is proportional to strain. Additionally, Fig. 10(a) shows that the stress–strain response for the two realizations of material (iii) are essentially identical. This suggests that the geometrically necessary dislocations determine the overall response, which is therefore insensitive to the precise distribution of the remaining statistically stored dislocations. At the same time, as seen in Fig. 12, there is a distinct size effect in this case. For material (i), on the other hand, where there are no geometrically necessary dislocations, the stress–strain response is governed by the statistically stored dislocations. The response in this case is sensitive to the particular distribution of sources and obstacles [8], and there is no size effect for this morphology.

To further link up our simulations with the concept of geometrically necessary dislocations, we briefly consider the density of such dislocations, ρ^G. For a row of plate-like particles subjected to shear, the density is estimated as [16]

$$\rho^G = \left(\frac{1}{\lambda^G}\right)\frac{2\Gamma}{b}$$

with λ^G equal to the spacing between particles (a three-dimensional estimate is obtained by replacing the factor 2 with 4). For the problem considered here, one could set λ^G equal to the spacing $2(w - w_f) = 2\sqrt{3}(1 - w_f/w)h$ (see Fig. 2) and estimate the relative density ρ^G/ρ from

$$\frac{\rho^G}{\rho} = \left(\frac{2\Gamma}{\rho L^2}\right)\left(\frac{L}{b}\right)\left(\frac{L}{\lambda^G}\right). \qquad (22)$$

All cases have used the same value of $L/b = 4000$, and ρL^2 is essentially proportional to Γ for material (iii) (see Figs 3, 10 and 12). The determination of the number of geometrically necessary dislocations from the actual distribution of dislocations at some strain level is not specified uniquely; as a working definition we have used the number of dislocations on either side of the central particle and within a distance of 0.1 times the particle spacing. The results obtained from equation (22) for both realizations of material (iii) (Fig. 10) agree reasonably well with the values of ρ^G/ρ obtained directly from Figs 6 and 11(a); for instance, we find $\rho^G/\rho \approx 0.3$ at $\Gamma = 0.96\%$, both according to equation (22) and to Fig. 6(b). Observing from Fig. 12 that $\rho L^2/\Gamma$ is about 40% higher for the case with the smaller particles ($h = L/2$), one would expect from equation (22) that the ratio ρ^G/ρ is a factor of roughly 1.4 larger for the smaller particles. Actually, counting gives $\rho^G/\rho \approx 0.4$ for $h = L/2$, which is a factor of 1.3 larger than that mentioned above for $h = L$. At least part of the small difference between the factors of 1.4 and 1.3 may be due to the arbitrariness in identifying geometrically necessary dislocations. At any rate, the size effect on the stress–strain behavior for this material is a consequence of a different density of geometrically necessary dislocations and possibly of a different ratio of geometrically necessary to total dislocations.

When counting geometrically necessary dislocations for material (ii) the same way as for material (iii), the value of ρ^G/ρ at $\Gamma = 1.0\%$ is 0.3. However, in this way some of the dislocations in the pile-ups emanating from the central particle (see Fig. 5) are identified as geometrically necessary and some as statistically stored. Because of these pile-ups, the identification of the fraction of geometrically necessary dislocations is not so clear cut in this case. If, alternatively, the dislocations in these pile-ups are completely disregarded in the counting, we find $\rho^G/\rho \approx 0.5$. This value is consistent with an estimate based on equation (22), using the dislocation density in Fig. 3.

The argument can also be reversed and equation (22) solved for the length scale λ^G as a function of dislocation density. This sort of characteristic length is important for gradient theories of plasticity [e.g. 19, 20]. For example, for material (i), where there are no geometrically necessary dislocations, λ^G is infinite, while for material (iii) one finds $\rho L^2/\Gamma \approx 8 \times 10^3$ from Fig. 10 so that $\lambda^G/L \approx \rho/\rho^G \approx 3$ (i.e. the length scale λ^G is about 3 μm for the material parameter values used here, see Section 3). A similar value is found for material (ii), when taking $\rho/\rho^G \approx 2$ as discussed above.

Both the discrete dislocation and continuum slip formulations predict that the proportion of the shear stress carried by the reinforcement, $\langle\sigma_{12}\rangle^*/\bar{\tau}$ in Table 1, is less for material (i) than for materials (ii) and (iii). Thus, according to both theories, when the reinforcement constrains plastic flow, the proportion of the load carried by the particles increases. However, the discrete dislocation results consistently predict a higher proportion of the stress carried by

the particle than is predicted by the continuum slip theory. As a consequence, in the bar charts in Figs 18 and 19, even for the larger window sizes, the continuum slip stress level is shifted to the right, since a greater fraction of the stress is carried by the matrix. Comparing the results in Table 1 for material (iii) with the two particle sizes, shows that the average stress in the particle increases with decreasing particle size, approximately in proportion with the increase in overall shear stress level.

The local stress concentration in the central particle is much higher for the discrete dislocation calculation than for the corresponding continuum slip calculation (Fig. 16). This is particularly the case for materials (ii) and (iii) where dislocation pile-ups occur at the particle–matrix interface. These high local stress concentrations are what lead to the higher average particle stresses. The significance of this result lies in the fact that it is the local stress distribution in the particles that is of relevance for reinforcement fracture. The local stress concentration is approximately the same for the material (iii) cases with different particle sizes. This suggests that the increasing propensity to particle fracture with increasing particle size seen experimentally [e.g. 21, 22], arises from an increased probability of having a critically sized flaw in larger particles rather than from an increase in particle stress level with particle size.

The differences in stress fields in the matrix obtained from the dislocation and continuum calculations, e.g. comparing Figs 7 and 8 with Fig. 15, are striking. With a view to the transition between dislocation-controlled to continuum-averaged plasticity descriptions, an obvious question to ask is: at what window size do the window-average stresses for the dislocation and continuum descriptions agree? In all cases (see Table 1), the proportion of the shear stress carried by the matrix is greater for the continuum description than for the discrete dislocation formulation. Moreover, the width of the continuum distributions is always less than that for the discrete dislocation distributions in Figs 18 and 19, at least for the particle sizes considered here. Presumably, the continuum results emerge in an appropriate limit; for example, with an increasing ratio of particle size to slip plane spacing or with an increasing ratio of particle size to mean dislocation spacing. However, over the range considered here, there is a systematic difference between the discrete dislocation and continuum plasticity predictions.

Another question is: what is the smallest window size for which the stress concentrations given by the continuum and dislocation solutions are in good agreement? This question has a more definite answer. For material (iii) with $h = L$ (Fig. 18), the continuum slip results provide a good estimate of the stress concentration down to A_w/A_m between 0.025 and 0.05. Using the value 0.05 and $A_m = 4\sqrt{3}L^2(1-f)$, the minimum size is $A_w = 0.28L^2$. Taking the square root of A_w, we get a characteristic size of about $0.5L$. On the other hand in Fig. 19, where $h = L/2$, the stress concentration factors from the two calculations are in agreement down to $A_w/A_m \approx 0.1$, which corresponds to $A_w = 0.14L^2$ and gives a characteristic size of about $0.4L$. Although not shown, bar charts for material (ii) show that the corresponding value of A_w/A_m is between 0.037 and 0.05. This leads again to a characteristic size of around $0.5L$. For $L = 1$ μm, the characteristic size at which the stress concentration can be estimated reasonably well with the continuum slip description is 0.4–0.5 μm.

It is of interest to relate this characteristic length to an intrinsic material length scale. In this respect it is noted that for both particle sizes in material (iii), the Burgers vector b was fixed and so was the spacing between slip planes, d. It is well known [1, 2] that a wall of dislocations, as builds up against the particle sides, gives rise to a short-range stress field that extends over a distance of the order of the spacing between dislocations in the wall, while the Burgers vector b sets the amplitude of the singular fields. This suggests relating the characteristic length to the dislocation spacing alongside the particles. For the larger strains [Fig. 6(b)], this spacing is almost equal to the spacing between slip planes, d, which is considered here as representative of the active slip plane spacing. Using this value, the above characteristic length is about 20 slip plane spacings.

6. CONCLUSIONS

- Microscale plastic flow in a composite material has been analyzed where matrix plasticity arises directly from the collective motion of large numbers of dislocations. Even though the dislocations are represented discretely, the formulation is a continuum one. The material hardening and the dislocation structure are outcomes of the boundary value problem solution.
- Although the boundary value problem analyzed is a highly idealized one, the results reproduce realistic features of the plastic response of metal–matrix composite materials.
- The role played by the material length scale, which enters the discrete dislocation formulation through the Burgers vector, depends on the reinforcement morphology. When the reinforcement blocks all matrix slip planes, the composite has high strain hardening and there is a significant size effect. On the other hand, when a vein of unreinforced matrix material is present, there is a yield point followed by a decrease in flow stress until a steady state is reached, and there is no size effect. Regardless of the reinforcement morphology, the composite hardening is size independent in classical continuum plasticity.

- The results suggest that continuum analyses of composite materials with micrometer size reinforcement may underestimate the stress carried by the reinforcing phase. Also, when the reinforcement blocks all slip planes, there is a high local stress concentration due to the dislocation pile-ups at the particle–matrix interface. These local stress concentrations, which are of significance for reinforcement fracture, are not represented by the continuum crystal plasticity solution.
- There is a range of size scales where the discrete dislocation formulation used here can yield insights into micro-scale plastic flow processes that are not amenable to either atomistic or conventional continuum analyses. The results also provide a basis for understanding the limits of conventional continuum formulations and for assigning the length scale associated with non-standard continuum theories [e.g. 19, 20, 23–25].

Acknowledgements—The work of HHMC is part of the research program of the "Stichting voor Fundamenteel Onderzoek der Materie (FOM)" which is supported financially by the "Nederlandse Organisatie voor Wetenschappelijk Onderzoek (NWO)". AN is grateful for support from the Air Force Office of Scientific Research under Grant F49620-94-1-0300. We are also pleased to acknowledge use of the workstation cluster at the Pittsburgh Supercomputer Center.

REFERENCES

1. Nabarro, F. R. N., *Theory of Crystal Dislocations*. Oxford University Press, Oxford, 1967.
2. Hirth, J. P. and Lothe, J., *Theory of Dislocations*. McGraw-Hill, New York, 1968.
3. Asaro, R. J., *Adv. appl. Mech.*, 1983, **23,** 1.
4. Bassani, J. L., *Adv. appl. Mech.*, 1994, **30,** 191.
5. Cuitiño, A. M. and Ortiz, M., *Model. Simul. Mater. Sci. Engng*, 1992, **1,** 225.
6. Peirce, D., Asaro, R. J. and Needleman, A., *Acta metall.*, 1983, **31,** 1951.
7. Van der Giessen, E. and Needleman, A., in *Computational Material Modeling*, ASME AD-Vol. 42/PVP-Vol. 294, ed. A. K. Noor and A. Needleman. ASME, New York, 1994, p. 53.
8. Van der Giessen, E. and Needleman, A., *Model. Simul. Mater. Sci. Engng*, 1995, **3,** 689.
9. Gulluoglu, A. N., Srolovitz, D. J., LeSar, R. and Lomdahl, P. S., *Scripta metall.*, 1989, **23,** 1347.
10. Amodeo, R. J. and Ghoniem, N. M., *Phys. Rev. B*, 1990, **41,** 6968.
11. Kubin, L. P., Canova, G., Condat, M., Devincre, B., Pontikis, V. and Bréchet, Y., in *Nonlinear Phenomena in Materials Science II*, ed. G. Martin and L. P. Kubin. Sci-Tech, Vaduz, 1992, p. 455.
12. Gulluoglu, A. N. and Hartley, C. S., *Model. Simul. Mater. Sci. Engng*, 1993, **1,** 383.
13. Fang, X. F. and Dahl, W., *Mater. Sci. Engng*, 1993, **A164,** 300.
14. Groma, I. and Pawley, G. S., *Mater. Sci. Engng*, 1993, **A164,** 306.
15. Lubarda, V., Blume, J. A. and Needleman, A., *Acta metall. mater.*, 1993, **41,** 625.
16. Ashby, M. F., *Phil. Mag.*, 1970, **21,** 399.
17. Rhee, M., Hirth, J. P. and Zbib, H. M., *Acta metall. mater.*, 1994, **42,** 2645.
18. Russell, K. C. and Ashby, M. F., *Acta metall.*, 1970, **18,** 891.
19. Fleck, N. A. and Hutchinson, J. W., *J. Mech. Phys. Solids*, 1993, **41,** 1825.
20. Fleck, N. A. and Hutchinson, J. W., *Adv. appl. Mech.*, in press.
21. Bre[faac]chet, Y., Newell, J., Tao, S. and Embury, D., *Scripta metall. mater.*, 1993, **28,** 47.
22. Finot, M., Shen, Y.-L., Needleman, A. and Suresh, S., *Metall. mater. trans.*, 1994, **25A,** 2403.
23. Walgraef, D. and Aifantis, E. C., *J. appl. Phys.*, 1985 **58,** 688.
24. Aifantis, E. C., *Mater. Sci. Engng*, 1986, **81,** 563.
25. De Borst, R., *Comp. Meth. appl. Mech. Engng*, 1993, **103,** 347.